IEEE Access
Multidisciplinary | Rapid Review | Open Access Journal

Received 4 October 2023, accepted 21 November 2023, date of publication 27 November 2023,
date of current version 5 December 2023.

Digital Object Identifier 10.1109/ACCESS.2023.3337079

RESEARCH ARTICLE

An Efficient OFDM-Based Monostatic Radar Design for Multitarget Detection

MAMADY DELAMOU[1], GUEVARA NOUBIR[2], (Senior Member, IEEE), SHUPING DANG[3], (Senior Member, IEEE), AND EL MEHDI AMHOUD[1], (Member, IEEE)

[1]College of Computing, Mohammed VI Polytechnic University, Benguerir, Salé 43150, Morocco
[2]Khoury College of Computer Sciences, Northeastern University, Boston, MA 02115, USA
[3]Department of Electrical and Electronic Engineering, University of Bristol, BS8 1UB Bristol, U.K.

Corresponding author: Mamady Delamou (mamady.delamou@um6p.ma)

This work was supported by the Junior Faculty Development Program under the UM6P–École Polytechnique Fédérale de Lausanne (EPFL) Excellence in Africa Initiative.

ABSTRACT In this paper, we propose a monostatic radar design for multitarget detection based on orthogonal-frequency division multiplexing (OFDM), where the monostatic radar is co-located with the transmit antenna. The monostatic antenna has the perfect knowledge of the transmitted signal and listens to echoes coming from the reflection of fixed or moving targets. We estimate the target parameters, i.e., range and velocity, using a two-dimensional (2D) periodogram. By this setup we improve the periodogram estimation performance under the condition of low signal-to-noise ratio (SNR) using Zadoff-Chu precoding (ZCP) and the discrete Fourier transform channel estimation (DFT-CE). Furthermore, since the dimensions of the data matrix can be much higher than the number of targets to be detected, we investigate the sparse Fourier transform-based Fourier projection-slice (FPS-SFT) algorithm and compare it to the 2D periodogram. An appropriate system parameterization in the industrial, scientific, and medical (ISM) band of 77 GHz, allows to achieve a range resolution of 30.52 cm and a velocity resolution of 66.79 cm/s.

INDEX TERMS Fourier slice theorem, joint communication and radar sensing (JCAS), monostatic radar, OFDM, Zadoff-Chu precoding.

I. INTRODUCTION

Wireless communication systems and radio sensing systems are two different engineering paradigms that have evolved separately in the past. However, nowadays, with the ever-increasing need for radio resources [1], implementing these two technologies separately leads to an inefficient utilization of the available spectrum. Despite their differences, communication and radar detection systems share many common features, particularly in terms of signal processing and equipment [2]. This has led several researchers to investigate the implementation of a unified system merging both technologies [3], [4], [5], [6], [7], [8]. Several approaches have been proposed in previous years, among which one of the prominent ideas is the coexistence of communications and radar detection [9], [10], [11]. By such a model, the radar and communication systems can be co-located and even physically integrated. However, they transmit two different signals that overlap in the time and/or frequency domains. To minimize the interference between them, both systems need to operate simultaneously by sharing the same resources in a cooperative way [2]. Nevertheless, with this coexistence, managing interference becomes a challenging task [9], [12]. In addition, another approach is to merge the communication and radar subsystems in a single device, using exactly the unified spectral and hardware resources. Such a conception is called in the literature joint communication and radar sensing (JCAS) or radio frequency (RF) convergence [13]. JCAS is significantly different from the aforementioned coexisting communication-radar systems. Instead, by JCAS, the same waveform is used for both communication and sensing. In such a design, many approaches can be considered. In [14], the authors proposed constant modulus waveforms for dual-function radar communication systems based on index modulation. The authors in [15] proposed a scheme that exploits constant-modulus and similarity constraints

The associate editor coordinating the review of this manuscript and approving it for publication was Sandra Costanzo.

to simultaneously integrate communication and sensing. In addition, in [16], the design proposed aims to simultaneously achieve a desired radar waveform in one spatial direction while transmitting an information-bearing communication signal in another spatial direction using the same antenna array. Another work presented in [17], introduced a novel approach called vehicular behavior-aware integrated sensing and communication. This approach involves steering beams based on vehicular behaviors to aid in driving tasks, while also facilitating spectral-efficient uplink data services through the assistance of a roadside unit.

Moreover, in [18] and [19], the authors demonstrate that WiFi or Zigbee signals could be used for object sensing as well, showing the possibility of exploiting communication signals for sensing (communication-centric design). This design strives to utilize the traditional communication waveforms directly or make certain alterations to achieve sensing capabilities concurrently. In such a design, the sensing information can be efficiently extracted from the echoes of the target, while ensuring the primary performance of the communication functionality [20]. As one of the pioneering works, the authors in [3] put forth a methodology that utilizes modulation symbols for signal processing in an integrated sensing and communication system based on orthogonal frequency division multiplexing (OFDM). In addition, in the approach proposed in [21], it was shown that the allocation of power, the number of OFDM subcarriers, the signal-to-noise ratio (SNR) per subcarrier are parameters that have an impact on sensing performance. In [22], the parameters of OFDM, such as the number of subcarriers, OFDM symbols, subcarrier interval, and pulse repetition interval, were designed to meet diverse sensing and communication requirements. Moreover, an alternative design was proposed in [23] to minimize the transmit power of each subcarrier while considering constraints related to conditional mutual information and data rates.

Furthermore, another design called sensing-centric or radar-centric leverages the sensing waveforms to enable secondary communication functionality concurrently. Radars, especially those used for military purposes are known for their remarkable long-range operation spanning hundreds of kilometers, they present a notable advantage when incorporating communication capabilities. This integration allows for the establishment of long-range communications. In [24], the authors consider the radar user as an active participant in the multiple-access channel. They derive the performance bounds for the coexistence of joint radar communications. In [25], the proposal involves the integration of a communication signal within the radar emission to achieve dual functionality. This is accomplished by selecting the radar transmit waveform from a bank of waveforms, where each waveform corresponds to a specific communication symbol, on a pulse-to-pulse basis. In addition, the study described in [26] emphasizes the utilization of time-modulated arrays presented as a means to achieve a dual-function array. This innovative approach enables the performance of radar functions in the main lobe while facilitating communication capabilities in the sidelobes of the array.

Given that OFDM has been widely adopted in contemporary mobile communication standards [27], [28], employing OFDM waveform for detection/radar purposes has attracted increasing interest in recent years [2], [29], [30], [31], [32]. In such a design, while the communication receiver needs to perform the channel estimation (CE) before decoding the transmitted data, the radar only needs to apply a detection algorithm on the reflected signal to estimate the range and velocity of targets.

In the field of parameter estimation, several detection algorithms have been proposed, among all target detection algorithms, the periodogram technique which is based on the discrete Fourier transform (DFT) was widely investigated [33]. The periodogram algorithm stands as a fundamental technique. In [34], the authors enhance our knowledge of the periodogram by exploring advanced techniques, such as non-uniform sampling and fast Fourier transform (FFT). In addition, the work proposed in [35] shows how the likelihood function can reveal the relationship between the carrier frequency offset and the periodogram of the received signal. This maximum likelihood has been developed based on zero-padded FFT, which is invoked for implementation. The author in [33] investigated the periodogram method, which is fundamentally based on the FFT. He showed that the maximum likelihood estimator could be derived for the case where there is exactly one target, which is anything but trivial. Furthermore, the authors in [36] presented spectral monitoring based on signal detection tools, by which the spectral components are estimated by the averaged periodogram non-parametric approach using an FFT.

In addition to the periodogram, there are several detection algorithms available for signal processing tasks. These algorithms offer different approaches and capabilities for parameter estimation and signal detection. One notable algorithm is the multiple signal classification (MUSIC) algorithm, which is based on eigenanalysis of the signal correlation matrix. MUSIC is particularly effective in identifying the frequencies of multiple sinusoidal components in a signal [37]. Another widely used algorithm is the estimation of signal parameters via rotational invariance technique (ESPRIT), which exploits the rotational invariance property of a uniform linear array to estimate the signal parameters [38]. Both MUSIC and ESPRIT are parametric methods that can provide good resolution in parameter estimation. However, it is important to consider that these algorithms typically require a large number of samples to achieve robust results [37], [38]. This requirement can pose challenges in scenarios where limited data is available or real-time processing is needed. Moreover, compressive sensing (CS) is another approach that has gained popularity in recent years [39], [40]. CS aims to reconstruct sparse signals from a small number of non-adaptive linear measurements. It offers an intriguing alternative to traditional signal processing

methods by exploiting the sparsity of signals in certain domains. However, the success of CS heavily relies on the sparsity assumption, and its performance may degrade if the underlying signal does not exhibit sufficient sparsity. Furthermore, the matrix pencil method can provide accurate results in some cases [41], it faces challenges when matching frequency pairs, which can lead to errors in parameter estimation. Some proposed techniques, such as the one described in Step 3 of Subalgorithm 1 in [42], aim to address this limitation by refining the matching process. However, further research and improvements are still needed to enhance the robustness and accuracy of the matrix pencil method in complex scenarios.

It is worth noting that despite their strengths, algorithms like MUSIC and ESPRIT suffer from high computational complexity. This computational burden can limit their practical applicability, particularly in real-time systems or resource-constrained environments. Additionally, the performance of these algorithms is heavily influenced by the SNR [43].

In this work, we propose a new design to integrate sensing to OFDM-based communications using co-located monostatic radars. In terms of sensing, we adopt the periodogram. The simplicity and computational efficiency of the periodogram have made it a widely used method in various signal processing applications. The periodogram algorithm is mainly computed using DFT and inverse discrete Fourier transform (IDFT). Ranges and velocities are contained in channel characteristics, which means that a precise estimation of these parameters by the radar system requires accurate channel state information. However, in the low SNR region, achieving an error-free channel estimate is a daunting task.

To overcome this challenge, we introduce the DFT-CE approach to reduce the false positive error in target selection. Additionally, we use Zadoff-Chu precoding (ZCP) and show that it can improve the estimation performance by ameliorating the SNR. Furthermore, even though using FFT and inverse fast Fourier transform (IFFT) to compute the periodogram is generally efficient, FFT/IFFT do not take into account the signal structure whereas a plethora of algorithms can be even faster by considering the signal sparsity [44], [45], [46], [47]. Consequently, we investigate the Fourier projection-slice (FPS)-sparse Fourier transform (SFT) [45] and discuss the trade-off to be taken between the estimation time and the estimation accuracy.

In sum, our main contributions in this paper are summarized as follows:

- By precoding the OFDM symbols with a Zadoff Chu code matrix, we first reduce the peak-to-average power ratio (PAPR) of the OFDM signal and then, decrease the estimation error of ranges and velocities in the low SNR region.
- Furthermore, DFT-CE is a channel estimation algorithm used to reduce the amount of noise in the frequency bin single-tap channel estimate. In this work, we adapt it to filter false positive targets. By combining it with ZCP, we come up with a better periodogram to accurately estimate targets' range and velocity.
- Finally, knowing that in practice the number of effective targets is smaller compared to the whole frame dimension, the signal is sparse in the frequency domain. We take advantage of this characteristic and apply the FPS-SFT to reduce the computational complexity along with the number of signal samples needed for estimation. By comparing it with the two-dimensional (2D) periodogram, we observe a compromise between the execution time and the accuracy in the low SNR region.

The remainder of this paper is organized as follows. In Section II, we introduce the problem statement, the system model, and the periodogram-based radar processing. Afterwards, we theoretically demonstrate the improvements, using the DFT-CE combined to ZCP and applying the FPS-SFT approach for reducing the computational complexity associated with the 2D periodogram processing in Section III. Simulation results and discussions are presented in Section IV. Finally, Section V concludes the work and sets forth our perspectives.

II. PROBLEM STATEMENT AND SYSTEM MODEL

A. PROBLEM STATEMENT

We consider a wireless communication system consisting of a communication antenna Tx co-located with a monostatic radar as depicted in Fig. 1. In the downlink, the signal emitted from the communication subsystem, is known to the radar, and is reflected by a certain number of targets characterized by their ranges and velocities. OFDM is one of the leading technologies used in contemporary wireless communication systems. Considerable attention has been given to OFDM for its performance advantages, such as its ability to mitigate inter carrier interference (ICI) and inter symbol interference (ISI) by making suitable use of a cyclic prefix (CP), as well as its robustness against frequency selective fading in addition to its efficient spectral utilization. In this regard, we adopt OFDM as the multiplexing scheme since using a single signal for communication and sensing is strongly dependent on the data structure [29]. The transmitted signal consists of pilots used for channel estimation and net information.

It is important to mention that channel estimation needs to be performed for both the communication and the radar subsystems, but in different ways and for different purposes. At the communication receiver, as usual, the received frequency-domain pilots are used to perform channel estimation using either least square (LS)-CE, minimum mean square error (MMSE)-CE, or any other channel estimation algorithms. Depending on the type of pilot arrangements, either frequency or time domain interpolation (or both) can be performed to infer the channel on the non-pilot subcarriers of each symbol [33], [48]. At the radar, which we treat in this work, the entire grid of the transmitted signal is used to perform the channel estimation [33], [48] since

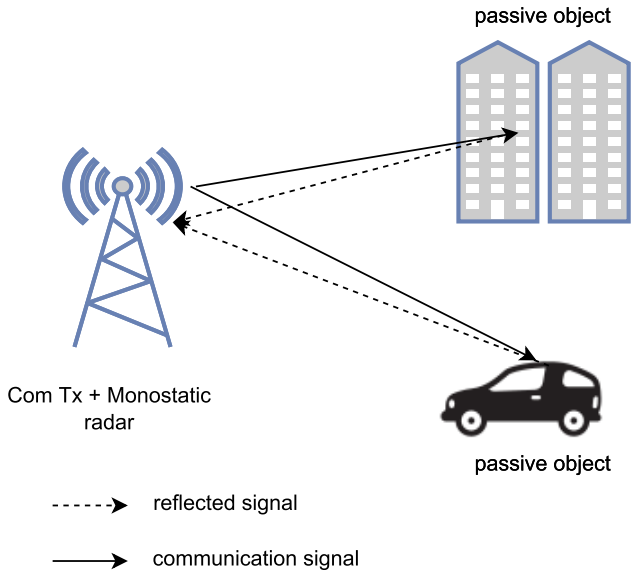

FIGURE 1. System model of the monostatic radar detection.

it knows the transmitted frames. The problem consists of estimating the channel to efficiently approximate the ranges and velocities of the targets using the reflected signals as shown in Fig. 1, and further, improve channel estimation. In this work, we focus on the downlink for simplicity, whereas most results and insights can be easily extended to the uplink. We also hypothesize that the interference between the radar and the communication antenna is negligible.

B. SYSTEM MODEL

In this section, we describe the communication and radar channel model and explain how the radar performs the target parameter estimation. We consider a total bandwidth B which can be divided into N small bands with central frequencies $f_0, f_1 \ldots f_{N-1}$ such that $\Delta f = \frac{B}{N}$. An OFDM symbol is a packet of N modulated data transmitted at the same time on $f_0, f_1 \ldots f_{N-1}$. The OFDM symbol duration T is thus given by $T = \frac{1}{\Delta f}$. After modulating bits by quadrature amplitude modulation (QAM), IFFT is applied to the QAM data symbols to generate OFDM waveforms in the time domain. Subsequently, a CP is added between consecutive symbols to mitigate ISI. Several OFDM waveforms are summed up to obtain an OFDM frame. The signal goes through a high power amplifier (HPA) and the communication antenna Tx transmits it. The channel is a multi-path channel, to which an additive white Gaussian noise (AWGN) is added. At the radar, inverse operations are executed. First, the CP is removed, and then FFT is performed on the OFDM bandpass signals. Finally, after the spectral division, the target detection algorithm is applied. The holistic process of transmission and detection is depicted in Fig. 2.

We assume that the complex symbols $\{a_{k,l}\}$ are generated after QAM modulation. Taking IFFT on the zeroth OFDM symbol $a_{k,0}$, the OFDM symbol sampled at sampling time $T_0 = \frac{T}{N}$ can be represented as [33]:

$$x[n] = x(nT_0) = \sum_{k=0}^{N-1} a_{k,0} e^{j2\pi \frac{nk}{N}}, \quad 0 \le n \le N-1, \quad (1)$$

which is the IFFT of the QAM symbols.

Taking into account the CP transmission time T_{cp}, an OFDM symbol transmission time T_s becomes $T_s = T + T_{cp}$. In terms of the number of symbols, we have $N_s = N + N_{cp}$, where N_{cp} is the number of complex symbols transmitted during T_{cp}. Assuming that an OFDM frame is composed of M OFDM symbols, the transmitted signal can be represented as:

$$x[n] = \sum_{l=0}^{M-1} \sum_{k=0}^{N-1} a_{k,l} e^{\frac{j2\pi k(n-lN_s)}{N}}. \quad (2)$$

1) RADAR CHANNEL MODEL

We consider a baseband signal $x(t)$ with carrier frequency f_c. The transmitted passband signal is $x_{pb}(t) = x(t)e^{j2\pi f_c t}$. For a given reflecting target at distance d from the transmitter and moving at velocity v, the received passband signal is impacted by [33]:

- Attenuation factor g which depends on distance d, radar cross section (RCS) σ_{RCS}, carrier frequency f_c and speed of light c, and by using the Friis equation of transmission, we obtain:

$$g = \sqrt{\frac{c\sigma_{RCS}}{(4\pi)^3 d^4 f_c^2}}. \quad (3)$$

- Signal delay τ caused by the round-trip, and $\tau = \frac{2d}{c}$.
- Doppler-Shift f_D caused by the velocity of the target, and $f_D = \frac{2v}{c} f_c$.
- Random rotation phase φ introduced when hitting the target.
- AWGN $z(t)$, and $z(t) \sim \mathcal{N}(\mu, \sigma^2)$.

Assuming a total number of N_t reflecting moving targets, and taking into account all the previous constraints, received passband signal $y_{pb}(t)$ is written as follows [48], [49]:

$$y_{pb}(t) = \sum_{p=0}^{N_t-1} g_p x(t - \alpha_p(t)) e^{j2\pi f_c(t-\alpha_p(t))} e^{j\varphi_p} + z_{pb}(t), \quad (4)$$

where $\alpha_p(t) = 2(\frac{d_p}{c} + \frac{v_p}{c}t) = \tau_p + B_p t$ and $B_p = 2\frac{v_p}{c}$.

At the radar, the received baseband signal $y(t)$ is obtained by demodulating y_{pb}(t) as $y(t) = y_{pb}(t)e^{-j2\pi f_c t}$. Thereafter, (4) can be rewritten as

$$y(t) = \sum_{p=0}^{N_t-1} g_p x(t - \alpha_p(t)) e^{-j2\pi f_c \tau_p t} e^{j2\pi f_{D_p} t} e^{j\varphi_p} + z(t). \quad (5)$$

Eq. (5) is the received signal containing attenuation g_p, channel delays τ_p, Doppler effects f_{D_p} and time-scale factor

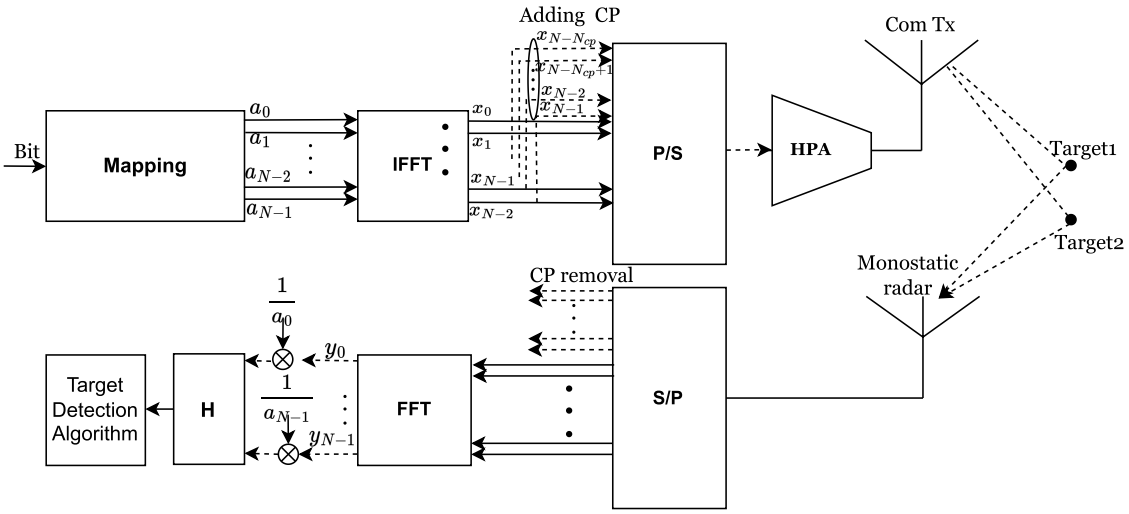

FIGURE 2. OFDM-based co-located monostatic radar transmission and detection process.

B_p. In essence, $y(t)$ is the filtered signal of $x(t)$ with the channel impulse:

$$h(t) = \sum_{p=0}^{N_t-1} g_p e^{-j2\pi f_c \tau_p} e^{j2\pi f_{D_p} t} e^{j\varphi_p} \delta\left((1-B_p)t - \tau_p\right), \quad (6)$$

where $\delta(t)$ is the Dirac function. A discrete-time counterpart considering a sample time T_0 is given by

$$h[n] = h(nT_0) = \sum_{p=0}^{N_t-1} g_p e^{-j2\pi f_c \tau_p} e^{j2\pi f_{D_p} nT_0} e^{j\varphi_p} \times \delta\left[(1-B_p)n - \tau_p/T_0\right]. \quad (7)$$

The discrete form of (5) can thus be written as

$$y[n] = x[n] \otimes h[n] + z[n], \quad (8)$$

where $\otimes$ is the convolution operation.

Knowing that $T_0 = \frac{1}{\Delta f N}$, the discrete-time counterpart of (5) can be obtained by introducing (7) and (2) in (8) [48]:

$$y[n] = \sum_{p=0}^{N_t-1} \sum_{l=0}^{M-1} \sum_{k=0}^{N-1} g_p a_{k,l} e^{j2\pi \frac{kn}{N}} e^{-j2\pi k \Delta f \tau_p} e^{\frac{-j2\pi k B_p n}{N}} \times e^{\frac{j2\pi k l N_s}{N}} e^{\frac{-j2\pi f_{D_p} n}{N\Delta f}} e^{j\varphi_p} + z[n]. \quad (9)$$

The signal for the lth OFDM symbol is expressed as

$$\begin{aligned} y[n,l] &= \sum_{p=0}^{N_t-1} \sum_{k=0}^{N-1} g_p a_{k,l} e^{j2\pi \frac{k(n-lN_s)}{N}} e^{-j2\pi k \Delta f \tau_p} \\ &\quad \times e^{\frac{-j2\pi k B_p (n-lN_s)}{N}} e^{\frac{j2\pi k l N_s}{N}} e^{\frac{-j2\pi f_{D_p}(n-lN_s)}{N\Delta f}} e^{j\varphi_p} + z[n]. \\ &= \sum_{p=0}^{N_t-1} \sum_{k=0}^{N-1} g_p a_{k,l} e^{j2\pi \frac{kn}{N}} e^{-j2\pi k \Delta f \tau_p} \\ &\quad \times e^{\frac{-j2\pi k B_p n}{N}} e^{\frac{j2\pi k B_p l N_s}{N}} e^{\frac{-j2\pi f_{D_p} n}{N\Delta f}} e^{\frac{j2\pi f_{D_p} l N_s}{N\Delta f}} e^{j\varphi_p} + z[n]. \end{aligned} \quad (10)$$

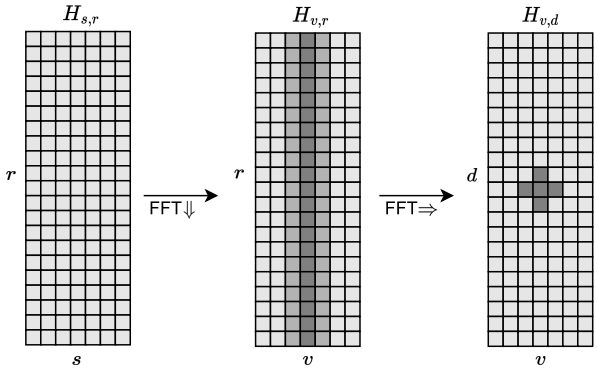

FIGURE 3. 2D periodogram computation process: The vertical ⇓ and horizontal ⇒ arrows indicate FFT over columns and rows, respectively.

According to [33], a large sub-carrier distance heavily alleviates the de-orthogonalizing effect of a frequency offset. Therefore, it must be ensured that Δf is larger than the Doppler shift caused by the object with the maximum relative velocity v_{max}, i.e.,

$$v_{max} \ll \frac{c\Delta f}{2f_c}, \quad (11)$$

which depends on the wave parameterization.

Our system parameterization satisfies (11), and, consequently, $(e^{\frac{-j2\pi k B_p n}{N}}, e^{\frac{j2\pi k B_p l N_s}{N}}, e^{\frac{-j2\pi f_{D_p} n}{N\Delta f}}) \longrightarrow (1,1,1)$. Therefore, (10) can be reduced to a simpler form infra:

$$y[n,l] = \sum_{p=0}^{N_t-1} \sum_{k=0}^{N-1} g_p a_{k,l} e^{j2\pi \frac{kn}{N}} e^{-j2\pi k \Delta f \tau_p} e^{\frac{j2\pi f_{D_p} l N_s}{N\Delta f}} e^{j\varphi_p} + z[n]. \quad (12)$$

2) RADAR PROCESSING

The main purpose of using the CP is to avoid ISI. For that, the maximum channel delay τ_{max} should be less than the cyclic

prefix transmission time, i.e.,

$$\max_{0\le p\le N_t-1}\{\tau_p\} \le T_{cp}. \tag{13}$$

We regulate that range d_{un} (respectively a velocity v_{un}) is unambiguous if two targets positioned at d and $d + d_{un}$ (respectively at moving velocities v and $v + v_{un}$) cannot be distinguished [33], given

$$d_{un} = \frac{c}{2\Delta f}, \text{ and } v_{un} = \frac{c}{2f_cT_s}. \tag{14}$$

A distance Δd (respectively velocity Δv) is called the radar resolution if it is the lowest distance (respectively velocity) such that two targets positioned at d and $d + \Delta d$ (respectively moving at velocities v and $v + \Delta v$) can still be distinguished [33], i.e.,

$$\Delta d = \frac{c}{2N\Delta f}, \text{ and } \Delta v = \frac{c}{2Mf_cT_s}. \tag{15}$$

The maximum range and the maximum velocity are directly defined by the parameters of the waveform as follows [33], [50]:

$$d_{max} = \frac{c \times T_{CP}}{2}, \text{ and } v_{max} \le \frac{c}{2f_cT_s}. \tag{16}$$

The first step of the estimation process is the spectral division. Since the radar knows the transmitted frames, the channel information can be retrieved by calculating the ratio of the whole received signal over the whole transmitted one, which results in the LS-CE estimate of the channel. Then, estimation matrix $\boldsymbol{H}$ has entries as follows:

$$h_{k,l} = \frac{y_{k,l}}{a_{k,l}} = \sum_{p=0}^{N_t-1} b_p e^{j2\pi \frac{lN_sf_{D_p}}{N\Delta f}} e^{-j2\pi k\Delta f\tau_p} e^{j\Phi} + \tilde{z}_{k,l}, \tag{17}$$

where $h_{k,l}$, $y_{k,l}$, $a_{k,l}$, and $z_{k,l}$ are the entry at the kth row and the lth column in matrix $\boldsymbol{H}$, received frame matrix $\boldsymbol{Y}$, transmitted frame matrix $\boldsymbol{A}$ and noise matrix $\tilde{\boldsymbol{Z}}$, respectively; Φ is the phase obtained after the element-wise division. A periodogram is an estimate of the spectral density of a signal. Since in our case $\boldsymbol{H}$ is a two-dimensional signal, the corresponding periodogram can also be written as [13]

$$P(s,r) = \frac{1}{NM}\left|\sum_{k=0}^{N'-1}\left(\sum_{l=0}^{M'-1} h_{k,l}w_{k,l}e^{-j2\pi\frac{ls}{R'}}\right)e^{j2\pi\frac{kr}{S'}}\right|^2, \tag{18}$$

where $r = 0, \ldots, N'-1$ and $s = \left\lfloor\frac{-M'}{2}\right\rfloor, \ldots, \left\lfloor\frac{M'}{2}\right\rfloor$-1. Here, $\left\lfloor\frac{M'}{2}\right\rfloor$ indicates the floor of $\frac{M'}{2}$, and the negative values of r allow estimating negative velocities. The problem here can be formulated as finding the optimal s and r in $\boldsymbol{P}$, by which the dominant frequencies are present. Those frequencies will represent the reflection points which are effective targets. In (18), $w_{k,l}$ is the value at the kth row and lth column in matrix $\boldsymbol{W}$. It is a window function that reduces the side-lobe levels of each dominant frequency. N' and M' are the extended values of N and M such that $N' \ge N$ and $M' \ge M$. N' and M' can improve the precision of the estimation but do not have any effect on the radar resolution. As such, (18) is equivalent to taking an M'-FFT of each column of $\boldsymbol{H}$ then an N'-IFFT of each row of the previously resulting matrix as depicted in Fig. 3. Consequently, (18) outputs dominant peaks, where targets are supposed to be located. Due to the whiteness of the noise, the detection threshold is equal to $\sigma^2\ln(P_{fa})$ [33]. More explicitly, as established in (19), any point (s, r) such that $P(s, r) \ge \sigma^2\ln(P_{fa})$ is considered as a target, otherwise it is regarded as noise, i.e., a false target, where P_{fa} is the desired probability of false alarm. Mathematically, we have

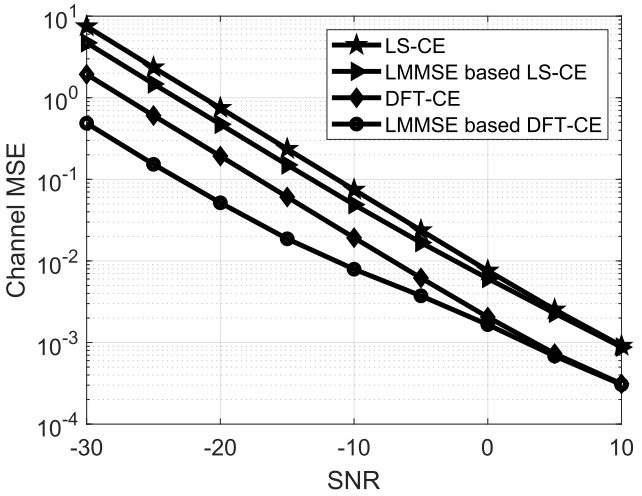

FIGURE 4. Channel MSE for LS-CE, LMMSE-based LS-CE, DFT-CE, and LMMSE-based DFT-CE.

$$P(s,r)\begin{cases}\ge \sigma^2\ln(P_{fa}), & \text{target}\\ \le \sigma^2\ln(P_{fa}), & \text{noise only}\end{cases}. \tag{19}$$

Once we obtain the list of estimates $\hat{s}$ and $\hat{r}$, the corresponding target range and velocity values are deduced as follows:

$$\hat{d}_p = \frac{c\hat{s}_p}{2N'\Delta f}, \text{ and } \hat{v}_p = \frac{c\hat{r}_p}{2f_cM'T_0}. \tag{20}$$

III. SENSING PERFORMANCE ENHANCEMENT

A. RADAR CHANNEL ESTIMATION USING DFT-CE

As presented previously, since targets' velocities and ranges can be extracted from the estimated channel information, the overall detection precision depends on the quality of $\boldsymbol{H}$ predicted using (17). The intuition is that an accurate estimation of $\boldsymbol{H}$ would output a precise parameter estimate. The approach that we propose below relies on the channel estimates using DFT-CE.

It is worth mentioning that the CP is longer than the maximum channel delay. As such, each path delay of the multipath channel is lower than the time required to transmit the CP. More explicitly, to estimate ranges and velocities,

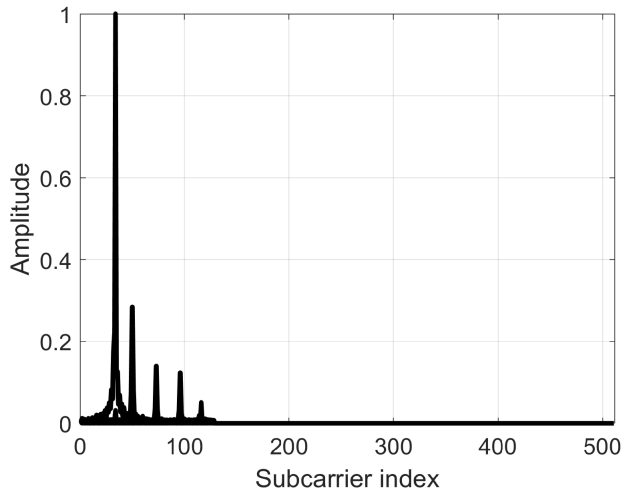

FIGURE 5. Periodogram's normalized peaks for 5 targets, given SNR = 0 dB, $N = 512$, and $N_{cp} = 128$.

instead of using all the channel impulse for the whole OFDM frame transmission time, we only use a short part of the channel impulse equivalent to the transmission time T_{CP}. At extremely low SNR, the noise level is higher than many targets' peaks. Thus, the periodogram can pick up wrong peaks as targets with a high probability. Using DFT-CE eliminates all the unuseful parts where targets are less likely to exist, which reduces the probability of the false detection caused by these peaks.

The DFT-CE process can essentially be performed in 3 steps [51]:

- Transform the frequency-domain channel $\boldsymbol{H}$ to the time domain using IFFT:

$$\hat{h}(n) = \frac{1}{K}\sum_{k=0}^{K-1} H(k)e^{j2\pi\frac{nk}{K}},\ 0 \le n \le K-1. \quad (21)$$

- Restrain the effect of noise by keeping only the cyclic prefix equivalent part of the signal:

$$\hat{h}_r(n) = \begin{cases} \hat{h}(n), & 0 \le n \le N_{cp}-1 \\ 0, & \text{otherwise} \end{cases} \quad (22)$$

- Convert the channel estimate back to the frequency domain using FFT:

$$\hat{H}'(k) = \frac{1}{K}\sum_{k=0}^{K-1} \hat{h}_r(n)e^{-j2\pi\frac{nk}{K}},\ 0 \le n \le K-1. \quad (23)$$

The operations of converting the frequency-domain channel to the time domain, then the time-domain channel back to the frequency-domain counterpart are fast since the IDFT and DFT are implemented through IFFT and FFT, respectively. This improves the efficiency of channel estimation with low complexity.

To obtain accurate channel state information, a better approach is to use MMSE-CE, which performs better than both LS-CE and DFT-CE. However, MMSE-CE is limited by its high complexity and also by the fact that we need real-time channel statistics (such as the covariance matrix), which are hard to know in practice. Even though in [51] the authors proposed MMSE based DFT-CE, which is faster than the MMSE-CE, its complexity remains very high and prohibitive for some applications when handling large matrices.

Fig. 4 depicts the estimated mean square error (MSE) of LS-CE, linear minimum mean square error (LMMSE) based LS-CE, DFT-CE, and LMMSE based DFT-CE. As shown in the figure, it is clear that LMMSE based DFT-CE outperforms the others followed by DFT-CE. In contrast, DFT-CE provides a good trade-off between desirable estimation performance (compared to LS-CE) and low complexity (compared to LMMSE based DFT-CE).

Fig. 5 and Fig. 6 present the levels of peaks according to OFDM subcarriers index for a five-target case. When SNR is high, all five targets are detectable, as shown in Fig. 5. However, knowing that targets can be located at subcarrier indexes i such that $0 \le i \le N_{cp}-1$, when SNR becomes very low, for instance SNR $= -25$ dB as presented in Fig. 6, some or all targets peaks are confused with the noise. Subsequently, they can be incorrectly selected in subcarrier index i, such that $i \ge N_{cp}-1$, which increases the detection errors as shown in Fig. 6. By applying DFT-CE, however, targets can still be erroneously selected in the right subcarrier index range, i.e., $0 \le i \le N_{cp}-1$, hence reducing the estimation errors as depicted in Fig. 6b.

B. ZADOFF-CHU PRECODING

Zadoff-Chu sequences are known as a polyphase complex-valued sequences with constant amplitude zero auto-correlation waveform (CAZAC). Because of their good auto-correlation properties, these sequences have many applications especially in 3GPP Long Term Evolution (LTE) for synchronization of mobile phones with base stations.

A Zadoff-Chu sequence of length L can be defined as:

$$Z_{seq}(k') = \begin{cases} e^{\frac{j2\pi r'}{L}\left(\frac{k'^2}{2}+q'k'\right)}, & \text{when } L \text{ is even} \\ e^{\frac{j2\pi r'}{L}\left(\frac{k'(k'+1)}{2}+q'k'\right)}, & \text{when } L \text{ is odd}, \end{cases} \quad (24)$$

where $k' = 0, 1, \ldots, L-1$; $q' \in \mathbb{Z}$; r' is an arbitrary integer relatively prime to L. From a Zadoff-Chu sequence of length L, we construct a square Zadoff-Chu matrix $\boldsymbol{Z_m}$ such that:

$$Z_{seq}(k') = Z_{seq}(iD+j) = Z_m(i,j),$$
$$0 \le i,j \le D-1, D = \sqrt{L}. \quad (25)$$

At the transmitter, we precode the QAM symbols by multiplying them with the matrix $\boldsymbol{Z_m}$. The precoded signal $\boldsymbol{A_p}$ is therefore $\boldsymbol{A_p} = \boldsymbol{Z_m A}$. At the receiver, the precoding can be discarded by multiplying the precoded received signal by $(\boldsymbol{Z_m})^{-1}$. It is important to mention that the precoding preserves the power of the signal $\boldsymbol{A}$ as we theoretically demonstrated in Appendix A. In addition, the IFFT operation

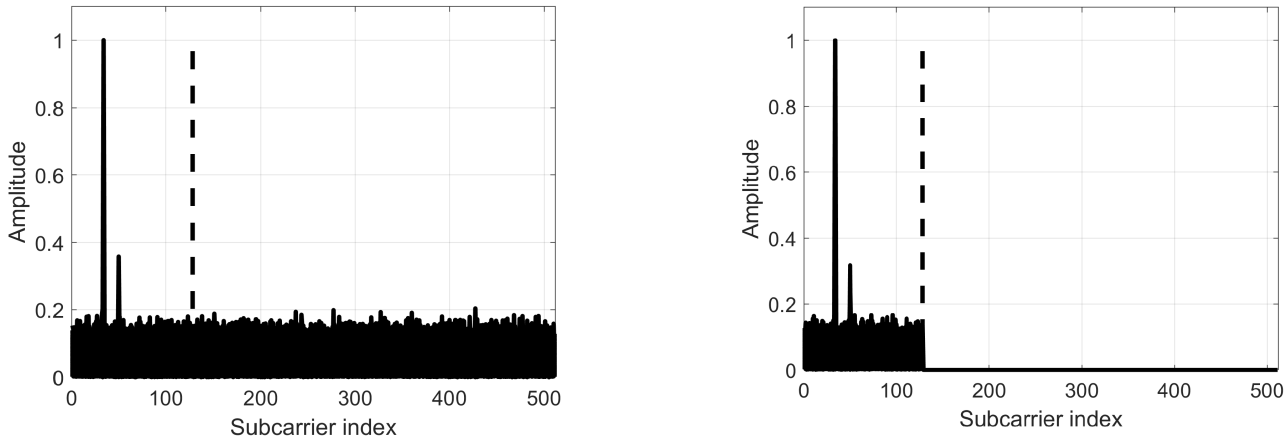

(a) LS-CE. (b) DFT-CE.

FIGURE 6. Normalized peak level as a function of the subcarrier index for 512-OFDM with $N_{cp} = 128$ and SNR = −25dB.

which follows the precoding converts the frequency-domain data into the time-domain representation and ensures that the subcarriers remain orthogonal to each other in the time domain. We provided mathematical proof of the power conservation after the IFFT operation using Parseval's energy conservation theorem in Appendix B. The PAPR of the signal obtained after this block is expressed as

$$PAPR = \frac{\max \|x\|^2}{E\left[\|x\|^2\right]}, \tag{26}$$

where x is the output signal.

One of the major drawbacks of OFDM is its high PAPR. An OFDM signal with high PAPR is highly sensitive to nonlinear distortion caused by an HPA. This distortion increases the adjacent channel interference (ACI) [52], [53]. Therefore PAPR reduction techniques may be employed to help cut it down. As demonstrated in [52], ZCP is used as a PAPR shrinking technique. Hence, from [52], we have the PAPR inequality expressed as

$$PAPR_{IFFT}(A_p) \leq PAPR_{IFFT}(A). \tag{27}$$

The CP adding operation which involves adding a copy of the end part of each OFDM symbol to the beginning of the symbol maintains the PAPR inequality at the output of the CP block. We provided these theoretical derivations in Appendix C. Furthermore, OFDM signals typically require high power levels for effective transmission, especially in scenarios with long-range or high-rate requirements. HPAs are utilized to amplify the OFDM signal to the desired power level for transmission. However, nonlinear HPAs can offer higher power efficiency compared to linear amplifiers. They can amplify the OFDM signal with less power consumption, which is advantageous in terms of energy efficiency and reducing operating costs.

In Fig. 7, we compute the spectrum of one QAM symbol in the 128-OFDM signal with $B = 20$ MHz, with an OFDM

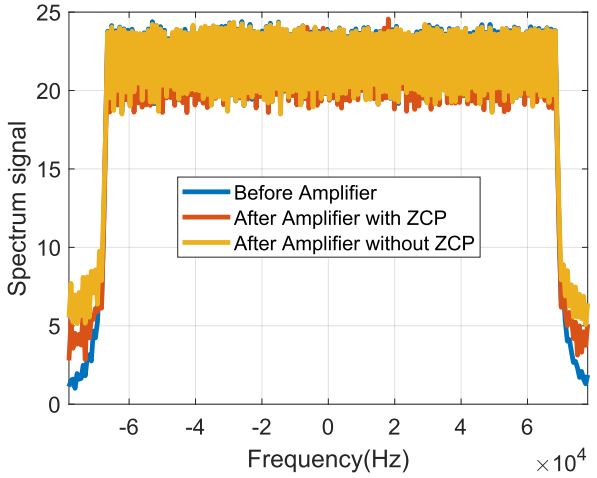

FIGURE 7. Spectrum of a single QAM symbol as a function of the frequency.

signal going through a nonlinear HPA with an output:

$$f_x = \frac{\|x\|}{\sqrt{1 + (\frac{\|x\|}{E(\|x\|)\times 10^{q/10}})^2}}, \tag{28}$$

with state level q; $\|x\|$ and $E(\|x\|)$ are the element-wise modulus of x and the mean of $\|x\|$, respectively; $\Delta f = \frac{B}{128}$. Here, each data symbol is within $[-\Delta f/2, \Delta f/2]$. As a result, the ACI of each modulated symbol in the OFDM-based ZCP, represented by the red curve is low compared to the ACI of the OFDM without ZCP illustrated by the yellow curve. Going through such an HPA maintains the PAPR inequality, which implies a better SNR in the radar channel. We thoroughly demonstrated this claim in Appendix D. In this work, we aim to analyze the impact of ZCP on the range and velocity estimations. By applying the previous ZCP on the OFDM signal, we end up with a signal with lower PAPR, lower ACI, high SNR and consequently, improved estimation of the range and velocity.

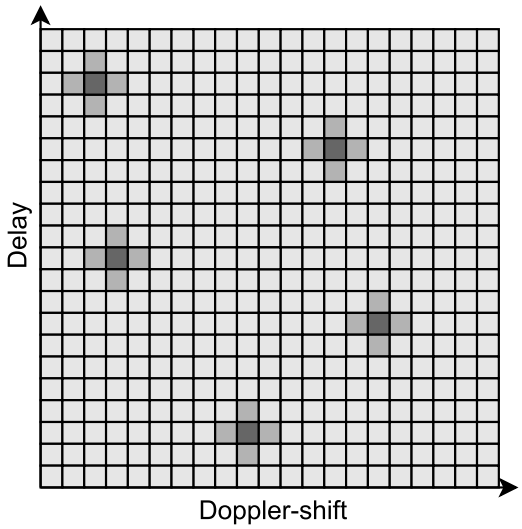

FIGURE 8. 2D sparse signal: The entire block is the signal frame, and each slot represents a potential target. The dark gray slots represent the effective targets.

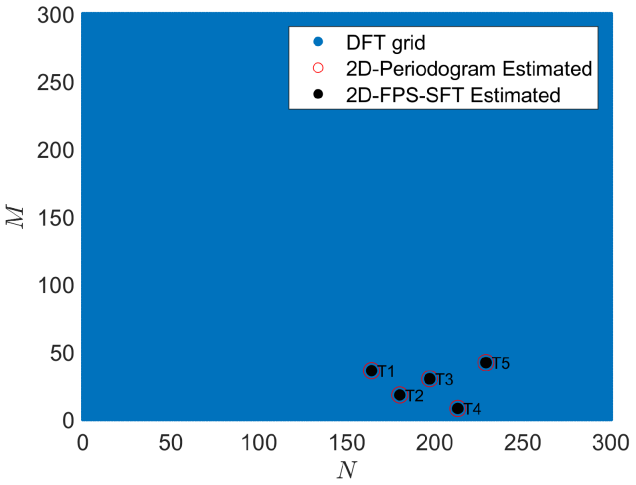

FIGURE 9. 2D periodogram and 2D-FPS-SFT estimate comparison for 5 targets with a 2048-OFDM, $M = 560$. Each target is identified by its coordinates (n, m).

C. COMPLEXITY REDUCTION

The DFT is one of the most important and widely used algorithms in computational tasks, such as in signal processing, communications, and audio/image/video compression. It is often implemented through FFT which computes the DFT of an n-dimensional signal with complexity $\mathcal{O}(n \log n)$. FFT does not make any assumption about the structure of the signal. However, in many applications, the signal is highly sparse in the frequency domain as depicted in Fig. 8. A signal x is exactly K-sparse (or approximately K-sparse) in the frequency domain if its Fourier transform contains exactly K non-zero values and the others are zeros. That is, the Fourier transform contains only K dominant values and the others are close to zero. In radar applications, only a few targets are of interest, such as buildings, trucks, and walls. Thus, the final output is often sparse.

Due to the importance of processing sparse data in many areas, several algorithms have been proposed to reduce not only the sampling complexity but also the computational complexity of FFT. A detailed study of such algorithms can be found in [44], [45], [46], and [47]. Some of these algorithms can even reach a computational complexity of $\mathcal{O}(K \log K)$ for exactly K-sparse signals. The basic principle of all SFT algorithms is to reduce the number of involved signal samples and the computational complexity. Thus, the significant frequencies in the signal are first localized and then estimated, either iteratively or simultaneously. However, most of these algorithms are only proposed for one-dimensional signals, and the extension of these algorithms to multi-dimensional signals is not straightforward. When dealing with multi-dimensional signals, it is required to create a large one-dimensional vector containing the entire signal. After the processing step, in order to return to the initial dimensions to determine the index of dominant frequencies. To alleviate many of the drawbacks brought by the aforementioned techniques, in [45], Wang et al. proposed FPS-SFT, which is a multi-dimensional and iterative SFT algorithm. It processes a multi-dimensional sparse signal with low complexity and small samples under both noise-free and noisy conditions. Consequently, since the signals interested in this paper are highly sparse ($K \ll N \times M$), in this subsection, we take a critical look at FPS-SFT algorithm in terms of its complexity and accuracy. The details of the algorithm can be found in [45]. Since FPS-SFT is iterative and the frequencies recovered in a given iteration are passed to the next iteration, in low SNR region, a frequency recovery error caused in a given iteration is carried through the next ones. Let us assume that the FPS-SFT algorithm executes I iterations and Q is the least common multiple of the signal dimensions N and M. For a general case of 2D signals, each iteration uses $3Q$ samples, since it is required that 3 Q-length slices are extracted to decode the two frequency components of a 2D signal in the frequency domain. Thus, the sampling complexity of FPS-SFT is $\mathcal{O}(3IQ) = \mathcal{O}(IQ)$. The core processing of FPS-SFT is the Q-point single-dimensional DFT, which can be implemented by the FFT with the computational complexity of $\mathcal{O}(Q \log Q)$. In addition to FFT, each iteration needs to evaluate up to Q samples corresponding to different frequencies. Hence, the computational complexity of FPS-SFT is $\mathcal{O}(I(Q \log Q + Q)) = \mathcal{O}(IQ \log Q)$. If we let the iteration size I equal I_{max} which is sufficiently large so that FPS-SFT converges for a given K-sparse signal, the sample and the computational complexity of FPS-SFT become $\mathcal{O}(Q)$ and $\mathcal{O}(Q \log Q)$, respectively. For $K = \mathcal{O}(Q)$, FPS-SFT achieves the lowest sample and computational complexity, i.e., $\mathcal{O}(K)$ and $\mathcal{O}(K \log K)$, respectively, among all considered SFT algorithms [45].

IV. SIMULATION RESULTS AND DISCUSSION

We evaluate the performance of the radar estimate in the industrial scientific and medical (ISM) band of 77 GHz for a total bandwidth of B = 491,52 MHz using the proposed algorithms. The simulation parameters are inspired by the

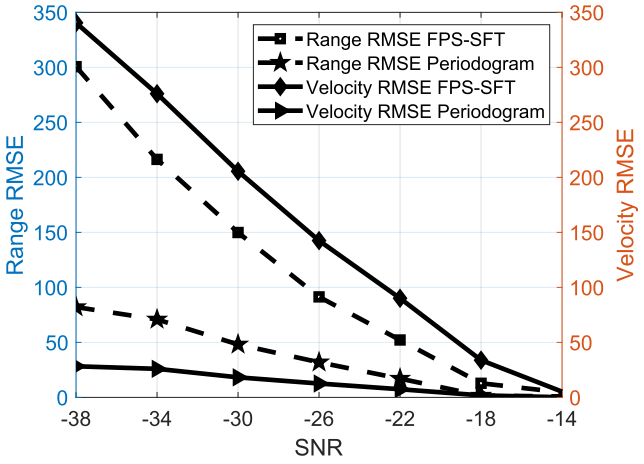

FIGURE 10. 2D-Periodogram and 2D-FPS-SFT estimate root mean square error (RMSE) as function of the SNR.

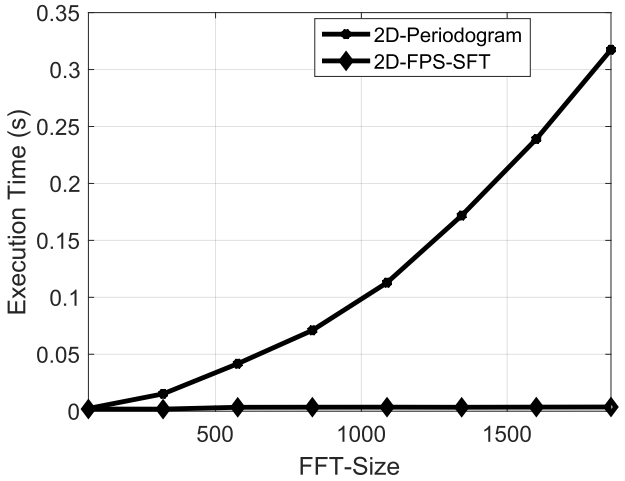

FIGURE 11. 2D periodogram and 2D-FPS-SFT execution time comparison with 5 targets versus the OFDM subcarrier number size, given $B = 60$ MHz and $M = 200$.

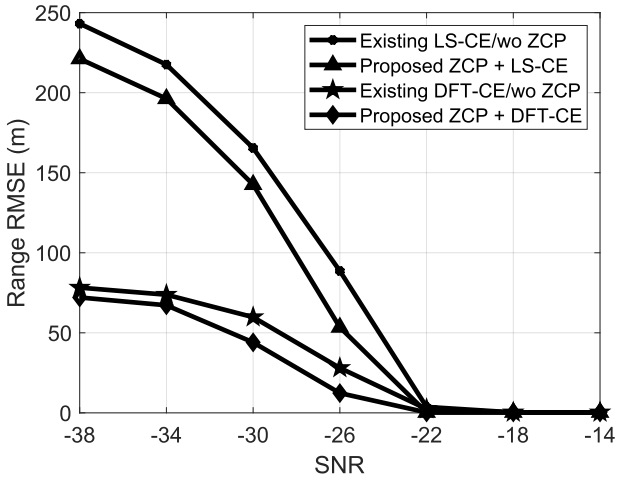

FIGURE 12. Range RMSE as a function of SNR for ZCP based LS-CE, LS-CE and DFT-CE.

TABLE 1. Simulation parameters.

Parameter	Symbol	Value
Number of OFDM symbols	M	560
Number of subcarriers	N	2,048
False alarm probability	P_{fa}	10^{-2}
Carrier frequency	f_c	77 GHz
Light speed	c	3×10^8 m/s
QAM-Size	–	16
Subcarrier space	Δf	240 KHz
Bandwidth	B	491.52 MHz
Slots per subframe	–	4
Maximum range	d_{max}	156.25 m
Maximum velocity	v_{max}	$\leq$ 374.05 m/s
Symbols per slot	–	14
Range resolution	Δd	30.52 cm
Velocity resolution	Δv	66.79 cm/s
Cyclic prefix	N_{cp}	512

5G New Radio (NR) specifications [54] and are summarized in Table 1. In 5G NR, each frame duration is 10 ms, corresponding to 10 subframes. The 240 KHz subcarrier spacing configuration contains 16 slots per subframe and 14 OFDM symbols by slot. Consequently, this gives a total of 2,240 OFDM symbols per frame with $T_{cp} = 7\% \times T$ (normal CP). This CP length is very small and can allow the radar to achieve only up to the coverage of $d_{max} = 43.73$ m. For the simplicity of our simulations, we stipulate 4 slots per subframe along with a CP such that $T_{cp} = 25\% \times T$, which results in a total of 560 OFDM symbols per frame and $d_{max} = 156.25$ m. In our simulations, we are assuming that all N OFDM subcarriers carry useful information except the first OFDM symbol of each frame, which contains block-type pilots for channel estimation at the communication receiver. We also assume that the multipath channel has a sufficiently long coherence time, which makes it unchanged during the transmission of an OFDM frame. The radar cross section is assumed to be unity. For the sake of simplicity, we further set N' and M' to be N and M, respectively. With $N = 2{,}048$ and $M = 560$. A Hamming window is used as the window function in (18). This configuration allows us to achieve a range resolution of 30.52 cm and a velocity resolution of 0.67 m/s. Such a radar can distinguish very close targets in terms of ranges and velocities. Thus, a good parameterization of the radar and wave characteristics is crucial to achieve good target detection performance.

Fig. 9 shows the ordinary periodogram and the FPS-SFT estimates of a five-sparse-signal case at SNR = 20 dB. We plot only the useful part of the signal where targets are located. From Fig. 9, we can observe that FPS-SFT and periodogram estimates perfectly match each other, which means that FPS-SFT can correctly estimate the dominant frequencies.

Fig. 10 depicts the RMSE of the targets' range and velocity estimation using FPS-SFT and 2D periodogram. From the figure, we observe that the 2D periodogram is more accurate than FPS-SFT in low SNR regions. However, both methods converge in the high SNR region.

Fig. 11 shows the execution time comparison of FPS-SFT and the periodogram. From the figure, we can notice that

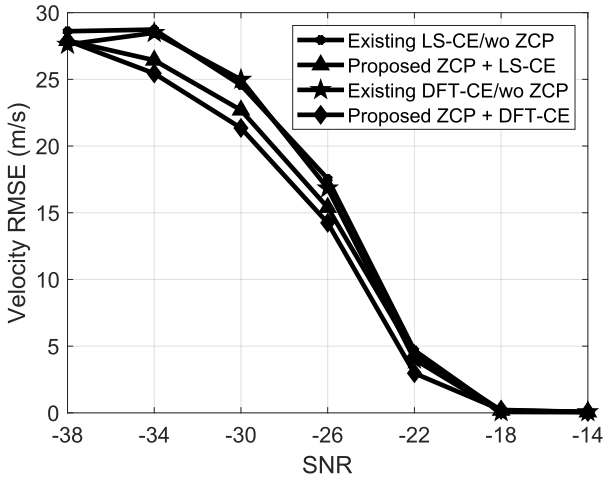

FIGURE 13. Velocity RMSE as a function of SNR for ZCP based LS-CE, LS-CE and DFT-CE.

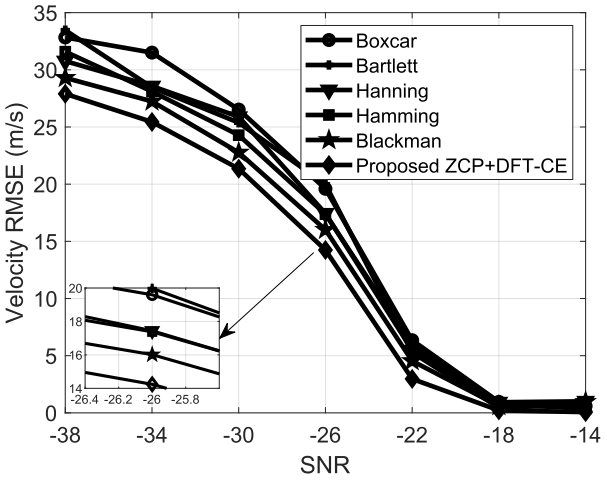

FIGURE 15. Velocity RMSE as a function of SNR for Boxcar, Bartlett, Hanning, Hamming, and Blackman window functions in comparison to the proposed scheme.

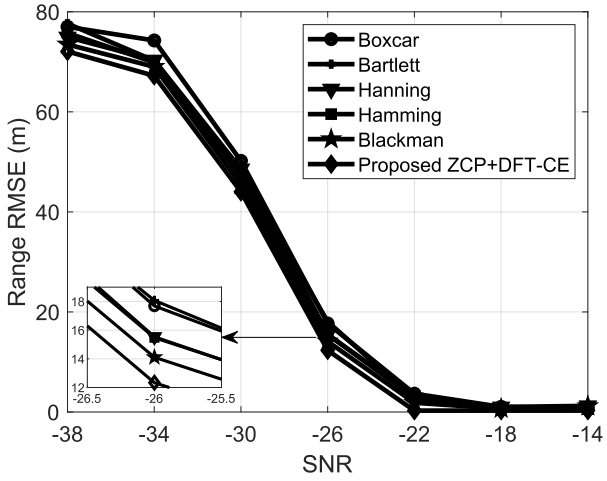

FIGURE 14. Range RMSE as a function of SNR for Boxcar, Bartlett, Hanning, Hamming, and Blackman window functions in comparison to the proposed scheme.

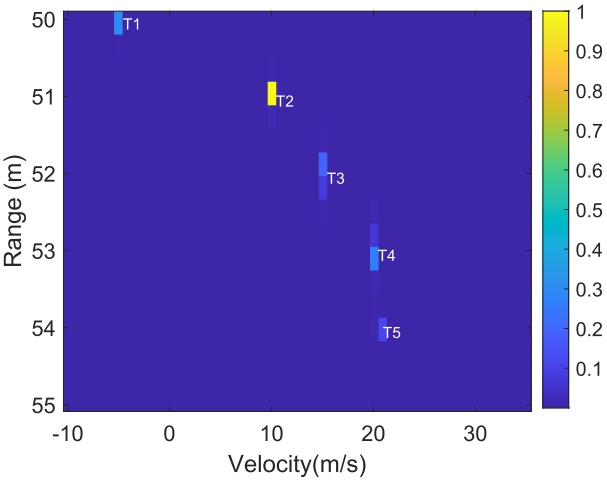

FIGURE 16. Radar image map for 5 targets within the ranges of 50 m, 51 m, 52 m, 53 m, 54 m and moving at the velocities of -5 m/s, 10 m/s, 15 m/s, 20 m/s, 21 m/s, with RCSs of 100 m^2, 350 m^2, 120 m^2, 150 m^2, 50 m^2, respectively, given SNR = 5 dB.

the periodogram execution time depends on the OFDM size, whereas FPS-SFT is almost constant only depending on the sparsity order K of the signal while drastically reducing the execution time.

From Fig. 10 and Fig. 11, we conclude that a compromise is to be taken between the accuracy and the complexity of both 2D periodogram and FPS-SFT depending on the type of application.

Fig. 12 and Fig. 13 show the RMSE of the range and velocity estimation for the standard periodogram using LS-CE and DFT-CE with and without ZCP. From these figures, we can observe that LS-CE, and DFT-CE using ZCP outperforms the case without ZCP. Moreover, applying DFT-CE based ZCP yields better estimates than LS-CE based ZCP. However, all the algorithms converge in higher SNR regions.

Fig. 14 and Fig. 15 show the RMSE of the range estimation for the classical periodogram using Boxcar, Bartlett, Hanning, Hamming, Blackman window functions and our proposed scheme. The figures depict the superior performance of our scheme compared to the classical window functions.

Fig. 16 shows a radar range-Doppler map, also called a radar image for five targets T_1, T_2, T_3, T_4, T_5 within the ranges of 50 m, 51 m, 52 m, 53 m, 54 m and moving at the velocities of -5 m/s, 10 m/s, 15 m/s, 20 m/s, 21 m/s, respectively, when SNR = 5 dB. According to [55], the RCS of a car at 77 GHz in decibel square meters is about 20 dBsm, which is equivalent to 100 m^2. Based on this value, we generated the five targets with RCSs equal to 100 m^2, 350 m^2, 120 m^2, 150 m^2, 50 m^2, respectively. These values align with potential representations of cars, trucks, and compact vehicles. The strongest reflecting target is T_2, because of its high RCS (more than three times the RCS of a car), which is similar to the signal reflected

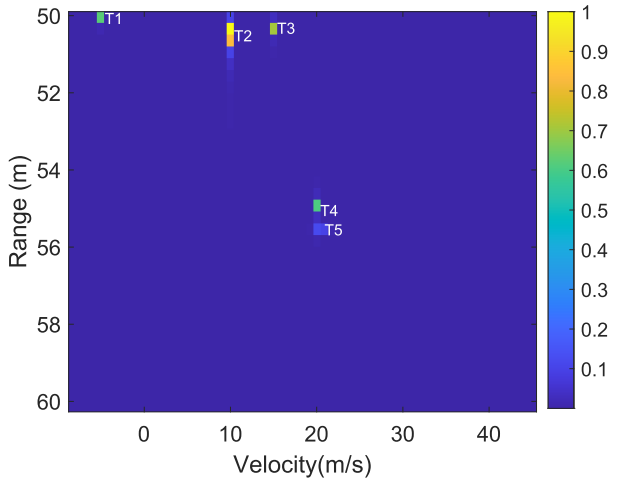

FIGURE 17. Radar image map for 5 targets within the ranges of 50 m, 50.5 m, 50.3 m, 55 m, 55.5 m and moving at the velocities of -5 m/s, 10 m/s, 15 m/s, 20 m/s, 20.5 m/s, with RCSs of 100 m^2, 350 m^2, 120 m^2, 150 m^2, 50 m^2, respectively, given SNR = 5 dB.

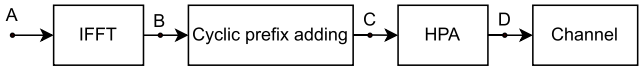

FIGURE 18. Transmitter blocks.

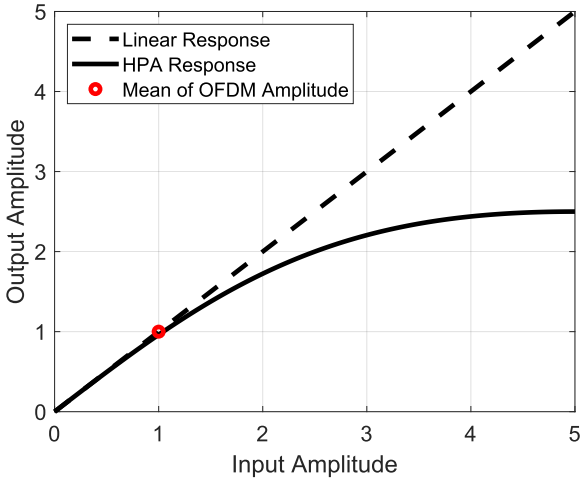

FIGURE 19. The output of the non-linear HPA.

by a truck. It is worth noting that all the targets are distinguishable in terms of range and velocity. This is because for any given two targets, the difference of their ranges (respectively velocities) is greater than the achievable range resolution (respectively velocity resolution) of the proposed scheme.

Fig. 17 shows the behavior of the proposed scheme in the case of close targets. Thoroughly, T_2 and T_3 are indistinguishable in terms of range. In fact, by projecting their main lobes on the range axis, they are perfectly aligned, which means that the radar can not see them as different targets in the range axis. This is because the difference of their ranges is less than the achievable range resolution Δd of the proposed scheme, $\Delta d_{T_2,T_3} = 50.5\ m - 50.3\ m = 20\ cm < \Delta d = 30.52\ cm$. In contrast, T_1, T_2, T_4, and T_5 are distinguishable in terms of range since the distance to each other is greater than Δd. Similarly, T_4 and T_5 are indistinguishable in terms of velocity, their main lobes are correctly aligned by projecting them on the velocity axis, this is because the difference of their respective velocities is less than the achievable velocity. $\Delta v_{T_5,T_4} = 20.5\ m/s - 20\ m/s = 50\ cm/s$, which is less than $\Delta v = 66.79\ cm/s$. In addition, T_1, T_2, T_3, and T_4 are distinguishable since the differences of their respective velocities are all greater than Δv.

V. CONCLUSION

In this work, we proposed an improved target detection method using several emergent techniques for the periodogram estimation proceeding. The periodogram algorithm outputs estimation in the limit of the radar resolution which depends on the signal parameterization. Through our simulations, we established that when dealing with low SNRs, the estimation using LS-CE performs poorly since the targets' peaks are confused with noise. By using DFT-CE, we improved the channel estimation and reduced the target estimation error by filtering some false positive targets. Moreover, we concluded that ZCP, in addition to its important applications in OFDM transmission for PAPR reduction and ICI alleviation, can also improve target estimation performance in low SNR region. Considering that received signals are often sparse, FPS-SFT effectively reduces the estimation complexity but has poor accuracy in low SNR regions. In our future works, we aim to apply a noise reduction method to Zadoff-Chu precoded signals to provide more accurate channel estimates at low SNR. An extended version of those algorithms could be applied to networks of unmanned aerial vehicles where targets are moving in three dimensions. Furthermore, the overall estimation performance can also be improved using machine learning, which could be a worthwhile research direction in the future.

APPENDIX A
PROOF OF THE POWER CONSERVATION BY THE ZADOFF-CHU PRECODING

Let us consider the OFDM QAM matrix $\mathbf{X} = (x)_{i,j}$, the precoded signal $\mathbf{Xp} = (x_p)_{i,j}$ is obtained by multiplying $\mathbf{X}$ with Zadoff-Chu matrix $\mathbf{Z} = (z)_{i,k}$ such as $\mathbf{X_p} = \mathbf{ZX}$, $1 \leq i, k \leq N$ and $1 \leq j \leq M$. We denote by $\|\cdot\|$ the Euclidean norm and by x_{ij}, $x_{p_{ij}}$, the ith row and jth column entry of matrices $(x)_{i,j}$ and $(x_p)_{i,j}$, respectively; z_{ik} is the ith row and kth column entry of matrix $(z)_{i,k}$, and, we have $\|z_{ik}\| = \frac{1}{\sqrt{N}}$.

We consider that $\mathbf{Z}$ is of dimension (N, N) and we denote by $\mathbf{X}^A$ with dimension (N, M), the signal at the point A in Fig. 18 (the signal before the IFFT). The precoding matrix is such that $\mathbf{X}_p^A = \mathbf{ZX}^A$. The ith row and kth column entry of matrix $\mathbf{X}_p^A$ can be written as $x_{p_{ik}}^A = \sum_{k=1}^{N} z_{ik} x_{kj}^A$.

Because of ZCP, the information on each subchannel is spread across all subchannels. It means that the power along the jth column of the matrix $(x)^A_{i,j}$ is the same as the one along the jth column of $(x_p)^A_{i,j}$. Therefore, this is mathematically expressed as

$$\lim_{v\to N}\sum_{i=1}^{v}\|x^A_{p_{ij}}\|^2=\lim_{v\to N}\sum_{i=1}^{v}\|x^A_{ij}\|^2. \tag{29}$$

The mean power of $\mathbf{X}^A$ and $\mathbf{X}^A_p$ are respectively expressed as follows

$$P_{\mathbf{X}^A}=\frac{\sum_{\substack{i=1\\j=1}}^{N,M}\|x^A_{ij}\|^2}{N\times M}\text{, and }P_{\mathbf{X}^A_p}=\frac{\sum_{\substack{i=1\\j=1}}^{N,M}\|x^A_{p_{ij}}\|^2}{N\times M}. \tag{30}$$

By rewriting the expression of $P_{\mathbf{X}^A_p}$ in (30) and substituting using the equation in (29), we obtain:

$$\begin{aligned}P_{\mathbf{X}^A_p}&=\frac{\sum_{\substack{i=1\\j=1}}^{N}\|x^A_{p_{ij}}\|^2}{N\times M}+\frac{\sum_{\substack{i=1\\j=2}}^{N}\|x^A_{p_{ij}}\|^2}{N\times M}\\&\quad+\cdots+\frac{\sum_{\substack{i=1\\j=M}}^{N}\|x^A_{p_{ij}}\|^2}{N\times M}\\&=\frac{\sum_{\substack{i=1\\j=1}}^{N}\|x^A_{ij}\|^2}{N\times M}+\frac{\sum_{\substack{i=1\\j=2}}^{N}\|x^A_{ij}\|^2}{N\times M}\\&\quad+\cdots+\frac{\sum_{\substack{i=1\\j=M}}^{N}\|x^A_{ij}\|^2}{N\times M}\\&=\frac{\sum_{\substack{i=1\\j=1}}^{N,M}\|x^A_{ij}\|^2}{N\times M}=P_{\mathbf{X}^A}.\end{aligned} \tag{31}$$

Hence, the signal power remains the same by precoding $\mathbf{X}^A$ by Zadoff-Chu matrix $\mathbf{Z}$.

APPENDIX B
PROOF OF THE POWER CONSERVATION BY THE IFFT

After the IFFT (at point B in Fig. 18), the energy conservation claim can be proven by using Parseval's energy conservation theorem. In the following, we denote

$$\mathbf{F}=\frac{1}{\sqrt{N}}\begin{bmatrix}1&1&\cdots&1\\1&W^2&\cdots&W^{N-1}\\1&W^2&\cdots&W^{2(N-1)}\\1&W^3&\cdots&W^{3(N-1)}\\\vdots&\vdots&\vdots&\vdots\\1&W^{N-1}&\cdots&W^{(N-1)(N-1)}\end{bmatrix},$$

where $W=e^{-j(2\pi/N)}$. In addition, $\mathbf{X}^B$ and $\mathbf{X}^B_p$ are the signals obtained after the IFFT operation on $\mathbf{X}^A$ and $\mathbf{X}_p$, respectively, as depicted in Fig. 18.

As indicated in [56], for any signal $\mathbf{X}$, the DFT and the IDFT can be viewed as a linear operator, and can be expressed respectively as

$$\mathbf{X}_{FFT}=\mathbf{F}\mathbf{X}\text{, and }\mathbf{X}=\mathbf{F}^{\dagger}\mathbf{X}_{FFT}, \tag{32}$$

where $\mathbf{F}^{\dagger}$ is the conjugate transpose of $\mathbf{F}$. As mentioned in [56], Parseval's energy conservation theorem states that:

$$\|X_{FFT}\|^2=\|X\|^2\Leftrightarrow\frac{\sum_{\substack{i=1\\j=M}}^{N,M}\|x_{ij}\|^2}{N\times M}=\frac{\sum_{\substack{i=1\\j=M}}^{N,M}\|x_{FFT_{ij}}\|^2}{N\times M}. \tag{33}$$

By applying (33) to $\mathbf{X}^B$ and $\mathbf{X}^B_p$, the energy of $\mathbf{X}^B$ and $\mathbf{X}^B_p$ are conserved after the IFFT, and by using (31), we derive that

$$P_{\mathbf{X}^B}=P_{\mathbf{X}^B_p}. \tag{34}$$

In addition, by denoting the PAPR function by $\mathscr{P}$, as shown in [52], after the IFFT, the following inequality holds:

$$\mathscr{P}(\mathbf{X}^B_p)\le\mathscr{P}(\mathbf{X}^B)\Leftrightarrow\frac{\max_{i,j}\|\mathbf{X}^B_p\|^2}{E[\|\mathbf{X}^B_p\|^2]}\le\frac{\max_{i,j}\|\mathbf{X}^B\|^2}{E[\|\mathbf{X}^B\|^2]}, \tag{35}$$

where $E[\|\mathbf{X}^B\|^2]=\frac{P_{\mathbf{X}^B}}{N\times M}$ and $E[\|\mathbf{X}^B_p\|^2]=\frac{P_{\mathbf{X}^B_p}}{N\times M}$. From (34), we have

$$E[\|\mathbf{X}^B\|^2]=E[\|\mathbf{X}^B_p\|^2]. \tag{36}$$

Therefore, based on (35) and (36), we can deduce that

$$\max_{i,j}\|\mathbf{X}^B_p\|^2\le\max_{i,j}\|\mathbf{X}^B\|^2. \tag{37}$$

APPENDIX C
ANALYSIS OF PAPR INEQUALITY AFTER ADDING CP

We consider the CP adding operation between B and C in Fig. 18. We denote by $\mathbf{X}^C$ and $\mathbf{X}^C_p$, the signals obtained after adding CP to $\mathbf{X}^B$ and $\mathbf{X}^B_p$, respectively. The CP adding operation consists of adding the last N_{cp} part of each OFDM symbol (each column of $\mathbf{X}^B$ and $\mathbf{X}^B_p$, respectively) at the beginning of the symbol. In addition, from $\mathbf{X}^B$ and $\mathbf{X}^B_p$ with the same dimension (N, M), we end up with $\mathbf{X}^C$ and $\mathbf{X}^C_p$ with dimensions $(N+N_{cp}, M)$.

- The inequality in (37) holds at C since the CP-adding operation extends the signal with elements selected from the same sample. Therefore,

$$\max_{i,j}\|\mathbf{X}^C_p\|^2\le\max_{i,j}\|\mathbf{X}^C\|^2. \tag{38}$$

- The mean power of $\mathbf{X}^C$ is expressed as

$$\begin{aligned}E[\|\mathbf{X}^C\|^2]&=\frac{N\times M}{(N+N_{cp})\times M}\frac{\sum_{\substack{i=1\\j=1}}^{N,M}\|x^B_{ij}\|^2}{N\times M}\\&\quad+\frac{N_{cp}\times M}{(N+N_{cp})\times M}\frac{\sum_{\substack{i=N+1\\j=1}}^{N+N_{cp},M}\|x^B_{ij}\|^2}{N_{cp}\times M}\\&=\frac{N\times M}{(N+N_{cp})\times M}E[\|X^B\|^2]\\&\quad+\frac{N_{cp}\times M}{(N+N_{cp})\times M}\frac{\sum_{\substack{i=N+1\\j=1}}^{N+N_{cp},M}\|x^B_{ij}\|^2}{N_{cp}\times M}.\end{aligned} \tag{39}$$

In the same way, the mean power of $\mathbf{X}_p^C$ is expressed as

$$\begin{aligned} E[\|\mathbf{X}_p^C\|^2] &= \frac{N \times M}{(N+N_{cp}) \times M} \frac{\sum_{i=1}^{N,M}{}_{j=1} \|x_{p_{ij}}^B\|^2}{N \times M} \\ &\quad + \frac{N_{cp} \times M}{(N+N_{cp}) \times M} \frac{\sum_{i=N+1}^{N+N_{cp},M}{}_{j=1} \|x_{p_{ij}}^B\|^2}{N_{cp} \times M} \\ &= \frac{N \times M}{(N+N_{cp}) \times M} E[\|X_p^B\|^2] \\ &\quad + \frac{N_{cp} \times M}{(N+N_{cp}) \times M} \frac{\sum_{i=N+1}^{N+N_{cp},M}{}_{j=1} \|x_{p_{ij}}^B\|^2}{N_{cp} \times M}. \end{aligned} \tag{40}$$

In this work, we take $N_{cp} = \frac{1}{4}N$. Therefore, from (29), we have

$$\frac{\sum_{i=N+1}^{N+N_{cp},M}{}_{j=1} \|x_{p_{ij}}^B\|^2}{N_{cp} \times M} \approx \frac{\sum_{i=N+1}^{N+N_{cp},M}{}_{j=1} \|x_{p_{ij}}^B\|^2}{N_{cp} \times M} \tag{41}$$

and from (36), the first terms of (39) and (40) are equal. Therefore, it can be approximated that

$$E[\|\mathbf{X}^C\|^2] \approx E[\|\mathbf{X}_p^C\|^2]. \tag{42}$$

Hence, by combining (38) and (42), we end up with

$$\mathscr{P}(\mathbf{X}_p^C) \leq \mathscr{P}(\mathbf{X}^C). \tag{43}$$

APPENDIX D
ANALYSIS OF PAPR INEQUALITY THROUGH AN HPA

We consider $\mathbf{X}^D$ and $\mathbf{X}_p^D$ the response of the HPA (at the point D in Fig. 18) taking $\mathbf{X}^C$ and $\mathbf{X}_p^C$ as the input, respectively. From (28), we have

$$\mathbf{X}^D = \frac{\|x\|}{\sqrt{1+(\frac{\|x\|}{E(\|x\|)\times 10^{q/10}})^2}}. \tag{44}$$

The state level of the HPA q is selected such that the output is the same as in Fig. 19. Therefore the HPA is a monotonic increasing function. Hence, for any entry $x_{p_{ij}}^C$ and $x_{p_{ij}}^C$, if $\|x_{p_{ij}}^C\| \leq \|x_{p_{ij}}^C\| \Rightarrow \|x_{p_{ij}}^D\| \leq \|x_{p_{ij}}^D\|$, from (42), we can deduce that

$$E[\|\mathbf{X}^D\|^2] \approx E[\|\mathbf{X}_p^D\|^2]. \tag{45}$$

Similarly, from (38), we can deduce that

$$\max_{i,j} \|\mathbf{X}_p^D\|^2 \leq \max_{i,j} \|\mathbf{X}^D\|^2. \tag{46}$$

Hence finally, from (45) and (46), we have

$$\frac{\max_{i,j}\|\mathbf{X}_p^D\|^2}{E[\|\mathbf{X}_p^D\|^2]} \leq \frac{\max_{i,j}\|\mathbf{X}^D\|^2}{E[\|\mathbf{X}^D\|^2]} \Leftrightarrow \mathscr{P}(\mathbf{X}_p^D) \leq \mathscr{P}(\mathbf{X}^D). \tag{47}$$

We normalize the transmitted signal with the maximum amplitude in each signal matrix. Such a normalization operation does not change the PAPR inequality. Consequently, for a given noise variance σ^2, we denote $\tilde{\mathbf{X}}_p^D$ and $\tilde{\mathbf{X}}^D$ the normalized signals. By definition, we have

$$SNR(\tilde{\mathbf{X}}_p^D) = \frac{E[\|\tilde{\mathbf{X}}_p^D\|^2]}{\sigma^2}. \tag{48}$$

In addition, we can write

$$\mathscr{P}(\tilde{\mathbf{X}}_p^D) = \frac{\max_{i,j}\|\tilde{\mathbf{X}}_p^D\|^2}{E[\|\tilde{\mathbf{X}}_p^D\|^2]} = \frac{1}{E[\|\tilde{\mathbf{X}}_p^D\|^2]}. \tag{49}$$

From (48) and (49), we have

$$SNR(\tilde{\mathbf{X}}_p^D) = \frac{1}{\sigma^2 \mathscr{P}(\tilde{\mathbf{X}}_p^D)}, \tag{50}$$

and knowing the inequality in (47), we obtain

$$\frac{1}{\sigma^2 \mathscr{P}(\tilde{\mathbf{X}}_p^D)} \geq \frac{1}{\sigma^2 \mathscr{P}(\tilde{\mathbf{X}}^D)} \Rightarrow SNR(\tilde{\mathbf{X}}_p^D) \geq SNR(\tilde{\mathbf{X}}^D). \tag{51}$$

Hence, ZCP increases the SNR in the radar channel.

REFERENCES

[1] M. Jouhari, N. Saeed, M.-S. Alouini, and E. M. Amhoud, "A survey on scalable LoRaWAN for massive IoT: Recent advances, potentials, and challenges," *IEEE Commun. Surveys Tuts.*, vol. 25, no. 3, pp. 1841–1876, 3rd Quart., 2023.

[2] M. L. Rahman, J. A. Zhang, K. Wu, X. Huang, Y. J. Guo, S. Chen, and J. Yuan, "Enabling joint communication and radio sensing in mobile networks—A survey," 2021, *arXiv:2006.07559*.

[3] C. Sturm and W. Wiesbeck, "Waveform design and signal processing aspects for fusion of wireless communications and radar sensing," *Proc. IEEE*, vol. 99, no. 7, pp. 1236–1259, Jul. 2011.

[4] A. Gameiro, D. Castanheira, J. Sanson, and P. P. Monteiro, "Research challenges, trends and applications for future joint radar communications systems," *Wireless Pers. Commun.*, vol. 100, no. 1, pp. 81–96, May 2018.

[5] M. L. Rahman, J. A. Zhang, X. Huang, Y. J. Guo, and R. W. Heath Jr., "Framework for a perceptive mobile network using joint communication and radar sensing," 2019, *arXiv:1901.05558*.

[6] A. Hassanien, M. G. Amin, E. Aboutanios, and B. Himed, "Dual-function radar communication systems: A solution to the spectrum congestion problem," *IEEE Signal Process. Mag.*, vol. 36, no. 5, pp. 115–126, Sep. 2019.

[7] L. Zheng, M. Lops, Y. C. Eldar, and X. Wang, "Radar and communication coexistence: An overview," *IEEE Signal Process. Mag.*, vol. 36, no. 5, pp. 85–99, Sep. 2019.

[8] M. Delamou, A. Bazzi, M. Chafii, and E. M. Amhoud, "Deep learning-based estimation for multitarget radar detection," in *Proc. IEEE 97th Veh. Technol. Conf. (VTC-Spring)*, Jun. 2023, pp. 1–5.

[9] F. Liu, C. Masouros, A. Li, and T. Ratnarajah, "Robust MIMO beamforming for cellular and radar coexistence," *IEEE Wireless Commun. Lett.*, vol. 6, no. 3, pp. 374–377, Jun. 2017.

[10] R. Saruthirathanaworakun, J. M. Peha, and L. M. Correia, "Opportunistic sharing between rotating radar and cellular," *IEEE J. Sel. Areas Commun.*, vol. 30, no. 10, pp. 1900–1910, Nov. 2012.

[11] A. F. Martone, K. A. Gallagher, and K. D. Sherbondy, "Joint radar and communication system optimization for spectrum sharing," in *Proc. IEEE Radar Conf. (RadarConf)*, Apr. 2019, pp. 1–6.

[12] E. Yousif, F. Khan, T. Ratnarajah, and M. Sellathurai, "On the spectral coexistence of colocated MIMO radars and wireless communications systems," in *Proc. IEEE 17th Int. Workshop Signal Process. Adv. Wireless Commun. (SPAWC)*, Jul. 2016, pp. 1–5.

[13] C. B. Barneto, L. Anttila, M. Fleischer, and M. Valkama, "OFDM radar with LTE waveform: Processing and performance," in *Proc. IEEE Radio Wireless Symp. (RWS)*, Jan. 2019, pp. 1–4.

[14] T. Huang, X. Xu, Y. Liu, N. Shlezinger, and Y. C. Eldar, "A dual-function radar communication system using index modulation," in *Proc. IEEE 20th Int. Workshop Signal Process. Adv. Wireless Commun. (SPAWC)*, Jul. 2019, pp. 1–5.

[15] C. G. Tsinos, A. Arora, S. Chatzinotas, and B. Ottersten, "Dual-function radar-communication systems with constant-modulus and similarity constraints," in *Proc. IEEE 12th Sensor Array Multichannel Signal Process. Workshop (SAM)*, Jun. 2022, pp. 231–235.
[16] P. M. McCormick, S. D. Blunt, and J. G. Metcalf, "Simultaneous radar and communications emissions from a common aperture—Part I: Theory," in *Proc. IEEE Radar Conf. (RadarConf)*, May 2017, pp. 1685–1690.
[17] D. Cong, S. Guo, S. Dang, and H. Zhang, "Vehicular behavior-aware beamforming design for integrated sensing and communication systems," *IEEE Trans. Intell. Transp. Syst.*, vol. 24, no. 6, pp. 5923–5935, Jun. 2023.
[18] J. Liu, G. Teng, and F. Hong, "Human activity sensing with wireless signals: A survey," *Sensors*, vol. 20, no. 4, p. 1210, Feb. 2020.
[19] S. Wang and G. Zhou, "A review on radio based activity recognition," *Digit. Commun. Netw.*, vol. 1, no. 1, pp. 20–29, Feb. 2015.
[20] W. Zhou, R. Zhang, G. Chen, and W. Wu, "Integrated sensing and communication waveform design: A survey," *IEEE Open J. Commun. Soc.*, vol. 3, pp. 1930–1949, 2022.
[21] Y. Liu, G. Liao, J. Xu, Z. Yang, and Y. Zhang, "Adaptive OFDM integrated radar and communications waveform design based on information theory," *IEEE Commun. Lett.*, vol. 21, no. 10, pp. 2174–2177, Oct. 2017.
[22] Y. Liu, G. Liao, Z. Yang, and J. Xu, "Design of integrated radar and communication system based on MIMO-OFDM waveform," *J. Syst. Eng. Electron.*, vol. 28, no. 4, pp. 669–680, Aug. 2017.
[23] C. Shi, F. Wang, S. Salous, and J. Zhou, "Low probability of intercept-based optimal OFDM waveform design strategy for an integrated radar and communications system," *IEEE Access*, vol. 6, pp. 57689–57699, 2018.
[24] A. R. Chiriyath, B. Paul, and D. W. Bliss, "Radar-communications convergence: Coexistence, cooperation, and co-design," *IEEE Trans. Cognit. Commun. Netw.*, vol. 3, no. 1, pp. 1–12, Mar. 2017.
[25] S. D. Blunt, M. R. Cook, and J. Stiles, "Embedding information into radar emissions via waveform implementation," in *Proc. Int. Waveform Diversity Design Conf.*, Aug. 2010, pp. 195–199.
[26] J. Euzière, R. Guinvarc'h, M. Lesturgie, B. Uguen, and R. Gillard, "Dual function radar communication time-modulated array," in *Proc. Int. Radar Conf.*, Oct. 2014, pp. 1–4.
[27] E.-M. Amhoud, M. Chafii, A. Nimr, and G. Fettweis, "OFDM with index modulation in orbital angular momentum multiplexed free space optical links," in *Proc. IEEE 93rd Veh. Technol. Conf. (VTC-Spring)*, Apr. 2021, pp. 1–5.
[28] K. Zerhouni, E. M. Amhoud, and M. Chafii, "Filtered multicarrier waveforms classification: A deep learning-based approach," *IEEE Access*, vol. 9, pp. 69426–69438, 2021.
[29] A. Evers and J. A. Jackson, "Analysis of an LTE waveform for radar applications," in *Proc. IEEE Radar Conf.*, May 2014, pp. 200–205.
[30] C. Sturm, T. Zwick, and W. Wiesbeck, "An OFDM system concept for joint radar and communications operations," in *Proc. VTC Spring IEEE 69th Veh. Technol. Conf.*, Apr. 2009, pp. 1–5.
[31] A. Zhang, Md. L. Rahman, X. Huang, Y. J. Guo, S. Chen, and R. W. Heath, "Perceptive mobile networks: Cellular networks with radio vision via joint communication and radar sensing," *IEEE Veh. Technol. Mag.*, vol. 16, no. 2, pp. 20–30, Jun. 2021.
[32] E.-M. Amhoud, G. R. Othman, and Y. Jaouën, "Concatenation of space-time coding and FEC for few-mode fiber systems," *IEEE Photon. Technol. Lett.*, vol. 29, no. 7, pp. 603–606, Apr. 2017.
[33] K. M. Braun, "OFDM radar algorithms in mobile communication networks," Ph.D. dissertation, Dept. Elect. Eng. Inf. Technol., Karlsruher Institut Für Technologie (KIT), Karlsruhe, Germany, 2014.
[34] P. Stoica and R. L. Moses, *Spectral Analysis of Signals*, vol. 452. Upper Saddle River, NJ, USA: Prentice-Hall, 2005.
[35] J. Lei and T.-S. Ng, "Periodogram-based carrier frequency offset estimation for orthogonal frequency division multiplexing applications," in *Proc. GLOBECOM01 IEEE Global Telecommun. Conf.*, Nov. 2001, pp. 3070–3074.
[36] V. Le Nir, T. van Waterschoot, M. Moonen, and J. Duplicy, "Spectral monitoring and parameter estimation for ZP-OFDM signals," in *Proc. 17th Eur. Signal Process. Conf.*, Aug. 2009, pp. 1898–1902.
[37] X. Wu, W.-P. Zhu, and J. Yan, "A fast gridless covariance matrix reconstruction method for one- and two-dimensional direction-of-arrival estimation," *IEEE Sensors J.*, vol. 17, no. 15, pp. 4916–4927, Aug. 2017.
[38] Y. Liu, G. Liao, Y. Chen, J. Xu, and Y. Yin, "Super-resolution range and velocity estimations with OFDM integrated radar and communications waveform," *IEEE Trans. Veh. Technol.*, vol. 69, no. 10, pp. 11659–11672, Oct. 2020.
[39] M. Davenport, M. Duarte, Y. Eldar, and G. Kutyniok, "Introduction to compressed sensing," *Preprint*, vol. 93, 01 2012.
[40] S. Ji, Y. Xue, and L. Carin, "Bayesian compressive sensing," *IEEE Trans. Signal Process.*, vol. 56, no. 6, pp. 2346–2356, Jun. 2008.
[41] Y. Hua, "Estimating two-dimensional frequencies by matrix enhancement and matrix pencil," *IEEE Trans. Signal Process.*, vol. 40, no. 9, pp. 2267–2280, Sep. 1992.
[42] A. Bazzi, D. T. M. Slock, and L. Meilhac, "Single snapshot joint estimation of angles and times of arrival: A 2D matrix pencil approach," in *Proc. IEEE Int. Conf. Commun. (ICC)*, May 2016, pp. 1–6.
[43] P. Pan, Y. Zhang, Z. Deng, and W. Qi, "Deep learning-based 2-D frequency estimation of multiple sinusoidals," *IEEE Trans. Neural Netw. Learn. Syst.*, vol. 33, no. 10, pp. 5429–5440, Oct. 2022.
[44] A. C. Gilbert, M. J. Strauss, and J. A. Tropp, "A tutorial on fast Fourier sampling," *IEEE Signal Process. Mag.*, vol. 25, no. 2, pp. 57–66, Mar. 2008.
[45] S. Wang, V. M. Patel, and A. Petropulu, "Multidimensional sparse Fourier transform based on the Fourier projection-slice theorem," *IEEE Trans. Signal Process.*, vol. 67, no. 1, pp. 54–69, Jan. 2019.
[46] P. Indyk, M. Kapralov, and E. Price, "(Nearly) sample-optimal sparse Fourier transform," in *Proc. 25th Annu. ACM-SIAM Symp. Discrete Algorithms*, Jan. 2014, pp. 480–499.
[47] B. Ghazi, H. Hassanieh, P. Indyk, D. Katabi, E. Price, and L. Shi, "Sample-optimal average-case sparse Fourier transform in two dimensions," in *Proc. 51st Annu. Allerton Conf. Commun., Control, Comput. (Allerton)*, Oct. 2013, pp. 1258–1265.
[48] I. Khelouani, K. Zerhouni, F. Elbahhar, R. Elassali, and N. Idboufker, "UFMC waveform and multiple-access techniques for 5G RadCom," *Electronics*, vol. 10, no. 7, p. 849, Apr. 2021.
[49] M. Braun, C. Sturm, and F. K. Jondral, "Maximum likelihood speed and distance estimation for OFDM radar," in *Proc. IEEE Radar Conf.*, May 2010, pp. 256–261.
[50] M. A. Richards, *Fundamentals of Radar Signal Processing*. New York, NY, USA: McGraw-Hill, 2014.
[51] J. Ma, H. Yu, and S. Liu, "The MMSE channel estimation based on DFT for OFDM system," in *Proc. 5th Int. Conf. Wireless Commun., Netw. Mobile Comput.*, Sep. 2009, pp. 1–4.
[52] I. Baig and V. Jeoti, "PAPR reduction in OFDM systems: Zadoff-Chu matrix transform based pre/post-coding techniques," in *Proc. 2nd Int. Conf. Comput. Intell., Commun. Syst. Netw.*, Jul. 2010, pp. 373–377.
[53] E.-M. Amhoud, G. R. Othman, L. Bigot, M. Song, E. R. Andresen, G. Labroille, M. Bigot-Astruc, and Y. Jaouen, "Experimental demonstration of space-time coding for MDL mitigation in few-mode fiber transmission systems," in *Proc. Eur. Conf. Opt. Commun. (ECOC)*, Sep. 2017, pp. 1–3.
[54] *5G; NR; Physical Channels and Modulation*, Standard 3GPP, TS 38.211 version 15.3.0 Release 15, ETSI, 2018.
[55] S. B. J. Gowdu, A. Schwind, R. Stephan, and M. A. Hein, "Monostatic RCS measurements of a passenger car mock-up at 77 GHz frequency in virtual environment," in *Proc. 16th Eur. Radar Conf. (EuRAD)*, Oct. 2019, pp. 361–364.
[56] M. Hassanzadeh and B. Shahrrava, "Linear version of Parseval's theorem," *IEEE Access*, vol. 10, pp. 27230–27241, 2022.

MAMADY DELAMOU received the M.S. degree in telecommunication and networking from the National Institute of Posts and Telecommunications, Rabat, in 2019. He is currently pursuing the Ph.D. degree with the School of Computer Science, Mohammed VI Polytechnic University (UM6P), Morocco. His research interests include wireless and wired communications, signal processing, radar detection, optimization problems, and artificial intelligence.

GUEVARA NOUBIR (Senior Member, IEEE) received the Ph.D. degree in computer science from the Swiss Federal Institute of Technology in Lausanne (EPFL), in 1996. He has held visiting research positions with Eurecom, MIT, and UNL. Prior to joining Northeastern University, he was a Senior Researcher with CSEM SA, from 1997 to 2000, where he led the design and development of the data protocol stack of the third-generation universal mobile telecommunication system (UMTS) and its world-first 3G prototype. His research led to a wide range of mechanisms and algorithms for scalable, secure, private, and robust wireless and mobile communications. His research covers both theoretical and practical aspects of privacy, security, and robustness in networked systems. He led the winning team of the 2013 DARPA Spectrum Cooperative Challenge against 90 academic and industry teams. He was a recipient of the National Science Foundation CAREER Award, in 2005; the ACM Conference on Security and Privacy in Wireless and Mobile Networks (WiSec) Best Paper Award, in 2011; and the Runner-Up Best Paper, in 2013. His research was featured in the NSF CISE/CNS Highlights in 2009 and 2012. He has served as the Program Co-Chair for many conferences in the areas of expertise, including the ACM Conference on Security and Privacy in Wireless and Mobile Networks, IEEE Conference on Communications and Network Security, and IEEE WoWMoM. He has co-chaired two NSF workshops on bio-computation and communications. He serves on the editorial board for the IEEE TRANSACTIONS ON MOBILE COMPUTING, the *Journal on Computer Networks* (Elsevier), and the *ACM Transactions on Information and System Security*.

SHUPING DANG (Senior Member, IEEE) received the first B.Eng. degree (Hons.) in electrical and electronic engineering from The University of Manchester, the second B.Eng. degree in electrical engineering and automation from Beijing Jiaotong University, in 2014, via a joint '2+2' dual-degree program, and the D.Phil. degree in engineering science from the University of Oxford, in 2018. He joined the Research and Development Center, Huanan Communication Company Ltd., after graduating from the University of Oxford. Then, he was a Postdoctoral Fellow with the Computer, Electrical and Mathematical Science and Engineering Division, King Abdullah University of Science and Technology (KAUST). He is currently a Lecturer with the Department of Electrical and Electronic Engineering, University of Bristol. His research interests include 6G communications, wireless communications, wireless security, and machine learning for communications.

EL MEHDI AMHOUD (Member, IEEE) received the Ph.D. degree in computer and communication sciences from Télécom ParisTech, France. He is currently an Assistant Professor with Mohammed VI Polytechnic University, Morocco. Prior to the current position, he was a Postdoctoral Research Fellow with the King Abdullah University of Science and Technology, Saudi Arabia. He holds several U.S. patents. His research interests include modeling and analyzing the performance of new generations of communication networks and the Internet of Things. He received two awards of excellence for the outstanding Ph.D. thesis from the Mines-Télécom Institute and the Marie Skłodowska-Curie Research Grant from the European Commission.